Title

CRISPR–Cas9-mediated nuclear transport and genomic integration of nanostructured genes in human primary cells

Permalink

Journal

ISSN

Authors

Lin-Shiao, Enrique
Pfeifer, Wolfgang G
Shy, Brian R
et al.

Publication Date

2022-02-22

DOI

Peer reviewed

CRISPR–Cas9-mediated nuclear transport and genomic integration of nanostructured genes in human primary cells

Enrique Lin-Shiao [1,2,†], Wolfgang G. Pfeifer [3,4,†], Brian R. Shy [5,6,7], Mohammad Saffari Doost [1,2], Evelyn Chen [1,2], Vivasvan S. Vykunta [5,6], Jennifer R. Hamilton [1,2], Elizabeth C. Stahl [1,2], Diana M. Lopez [3,8,9], Cindy R. Sandoval Espinoza [1,2], Alexander E. Deyanov [1,2], Rachel J. Lew [1,2,6], Michael G. Poirer [4,8,9], Alexander Marson [5,6], Carlos E. Castro [3,8] and Jennifer A. Doudna [1,2,6,10,11,12,13,14,*]

[1]Department of Molecular and Cell Biology, University of California, Berkeley, Berkeley, CA 94720, USA, [2]Innovative Genomics Institute, University of California, Berkeley, Berkeley, CA 94720, USA, [3]Department of Mechanical and Aerospace Engineering, The Ohio State University, Columbus, OH 43210, USA, [4]Department of Physics, The Ohio State University, Columbus, OH 43210, USA, [5]Department of Medicine, University of California, San Francisco, San Francisco, CA 94143, USA, [6]Gladstone-UCSF Institute of Genomic Immunology, San Francisco, CA 94158, USA, [7]Department of Laboratory Medicine, University of California, San Francisco, San Francisco, CA 94143, USA, [8]Biophysics Graduate Program, The Ohio State University, Columbus, OH 43210, USA, [9]Department of Chemistry and Biochemistry, The Ohio State University, Columbus, OH 43210, USA, [10]Howard Hughes Medical Institute, University of California, Berkeley, Berkeley, CA 94720, USA, [11]Department of Chemistry, University of California, Berkeley, Berkeley, CA 94720, USA, [12]Molecular Biophysics and Integrated Bioimaging Division, Lawrence Berkeley National Laboratory, Berkeley 94720, CA, USA, [13]California Institute for Quantitative Biosciences (QB3), University of California, Berkeley, Berkeley, CA 94720, USA and [14]Gladstone Institutes, University of California, San Francisco, San Francisco, CA, 94158, USA

ABSTRACT

DNA nanostructures are a promising tool to deliver molecular payloads to cells. DNA origami structures, where long single-stranded DNA is folded into a compact nanostructure, present an attractive approach to package genes; however, effective delivery of genetic material into cell nuclei has remained a critical challenge. Here, we describe the use of DNA nanostructures encoding an intact human gene and a fluorescent protein encoding gene as compact templates for gene integration by CRISPR-mediated homology-directed repair (HDR). Our design includes CRISPR–Cas9 ribonucleoprotein binding sites on DNA nanostructures to increase shuttling into the nucleus. We demonstrate efficient shuttling and genomic integration of DNA nanostructures using transfection and electroporation. These nanostructured templates display lower toxicity and higher insertion efficiency compared to unstructured double-stranded DNA templates in human primary cells. Furthermore, our study validates virus-like particles as an efficient method of DNA nanostructure delivery, opening the possibility of delivering nanostructures *in vivo* to specific cell types. Together, these results provide new approaches to gene delivery with DNA nanostructures and establish their use as HDR templates, exploiting both their design features and their ability to encode genetic information. This work also opens a door to translate other DNA nanodevice functions, such as biosensing, into cell nuclei.

*To whom correspondence should be addressed. Tel: +1 510 643 0108; Fax: +1 510 643 0080; Email: doudna@berkeley.edu
†The authors wish it to be known that, in their opinion, the first two authors should be regarded as Joint First Authors.
Present address: Enrique Lin-Shiao, BridgeBio Pharma, Palo Alto, CA 94301, USA.

INTRODUCTION

Programmed self-assembly of DNA nanostructures (1–5) has applications in nanomanufacturing (6), biosensing (7) and biophysics (8–10). While in cell and *in vivo* applications of DNA nanostructures have been explored, progress has been hampered by challenges including uptake and stability of structures in cells (11,12). Previous work showed that DNA nanostructures remain stable in cell lysate for up to 24 h and a single study has demonstrated cytosolic delivery with electrotransfection (13).

The scaffolded DNA origami approach (3) is particularly well suited to package sequences of several kilobases into a compact nanostructure. Because these DNA nanostructures are agnostic to the underlying DNA sequence, structures that exploit both their design features and their ability to encode genetic information can be engineered. This offers a promising route for nanostructure-mediated gene delivery. While previous efforts have demonstrated the ability to effectively deliver small molecules (14,15), peptides and proteins (16,17), and nucleic acids such as siRNA (18,19) and prokaryotic genes (20) to cells, these studies require delivery to the cell surface or cytoplasm. Delivery of genomic information to the nucleus has remained a key challenge. Ideally, a nanostructure gene delivery system could target a gene to a specific genome site for integration.

CRISPR–Cas9 homology-directed repair (HDR) thus offers an attractive route since the gene of interest can be targeted through the inclusions of homologous sequences of DNA, which are straightforward to include on a DNA nanostructure. Furthermore, DNA nanostructures could offer a route for developing improved HDR templates for genome engineering. For example, long single-stranded DNA (ssDNA) donor templates can be folded to co-localize terminal sequences bearing homology to the intended genomic insertion site (homology arms). In addition, nanostructures can create compaction that could improve cellular delivery, increase half-life and circumvent toxicity of free DNA. Despite this promise for gene delivery with DNA nanostructures, several key advances are yet to be demonstrated, including packaging of genes, effective delivery to the nucleus of live cells, integration of nanostructured genetic material into the genome and targeting exogenous genes to a genome site of interest.

In this study, we tested strategies for nuclear delivery of DNA nanostructures encoding genes that can be used as HDR donor templates for precise, large genomic insertions using CRISPR–Cas9. Comparison of different methods for DNA introduction into cells showed electroporation to be an effective delivery strategy. DNA nanostructures with short terminal sequences matching the sequence of the genomic integration site increased genomic insertion efficiency induced by Cas9 ribonucleoproteins (RNPs) compared to unstructured double-stranded DNA (dsDNA). This strategy was used in primary human T cells to replace a defective copy of *IL2RA*, a gene mutated in a familial immune dysregulation syndrome. We also tested Cas9 virus-like particles (Cas9-VLPs) for the co-delivery of DNA nanostructures, finding that relative to unstructured DNA templates, nanostructured DNA templates doubled the observed Cas9-induced genomic integration efficiency. These results demonstrate the utility of DNA nanostructures for some applications of genome editing and suggest that DNA template structure may assist both the delivery and use of DNA in other therapeutic and bioimaging applications. Furthermore, the ability to deliver DNA nanostructures to cell nuclei opens a door to translate other functions of DNA nanotechnology to the nucleus, such as force sensing (21), molecular detection (22) and biophysical measurement (23).

MATERIALS AND METHODS

ssDNA production

Biotin-labeled dsDNA template was first amplified from the plasmid encoding the template design with biotin-labeled primers using KAPA HiFi HotStart ReadyMix PCR Kit (Roche) for 35 cycles (98°C for 20 s, 65°C for 15 s and 72°C for 1 min; then 72°C for 1 min). dsDNA was then purified and concentrated by mixing with $1.8\times$ sample volume of SPRI beads (UC Berkeley Sequencing Core). The samples were placed on a DynaMag-2 magnet (Thermo Fisher Scientific) for 5 min, and the supernatant was removed. The samples were washed twice with 70% ethanol and eluted in Tris–EDTA buffer (Corning).

ssDNA was prepared by separating dsDNA strands using Dynabeads MyOne Streptavidin C1 beads (Thermo Fisher Scientific). Streptavidin beads were first washed three times with 1 ml $1\times$ binding and washing (B&W) buffer ($2\times$ B&W buffer: 10 mM Tris–HCl, pH 7.5, 1 mM EDTA, 2.0 M NaCl). dsDNA was added to streptavidin beads and rotated for 30 min at room temperature. Beads were then collected on a magnet and washed once with $1\times$ B&W buffer. Next, beads were resuspended in 2×100 μl melt buffer (125 mM NaOH in ddH_2O), incubated for 2 min and immediately precipitated, and the supernatant was transferred to a new nonstick 1.5-ml microcentrifuge tube containing 1 ml neutralization buffer (60 mM sodium acetate in TE buffer, pH 8.0). The supernatant containing ssDNA was purified using SPRI beads and eluted in ddH_2O.

Folding and purification of DNA nanostructures

DNA nanostructures were folded by mixing 10 nM ssDNA HDR template with 100 nM of each staple strand in $1\times$ TEMg buffer (5 mM Tris, 1 mM EDTA, 8 mM $MgCl_2$, pH 8). The thermal annealing protocol starts with a heat denaturation step at 65°C to remove any undesired secondary structure and then gradually decreases over the course of 14 h to 20°C (Supplementary Table S1). DNA nanostructures were subsequently purified and concentrated by five to six rounds of spin filtration (Amicon 100 kDa) at 5000 rcf following previously reported protocols (24). Samples for atomic force microscopy (AFM) imaging were purified by using the Freeze 'N Squeeze (Bio-Rad) gel extraction kit according to the manufacturer's protocol. Briefly, target bands were excised from agarose gels, placed into the respective spin columns and spun at 13 000 rcf for 5 min.

Agarose gel electrophoresis

Proper folding of DNA nanostructures was confirmed using agarose gel electrophoresis. One hundred fifty femto-

moles of folded sample was loaded into agarose gels [1.5% agarose, $1\times$ TBEMg (45 mM Tris, 45 mM boric acid, 1 mM EDTA, 11 mM $MgCl_2$, pH 8), containing ethidium bromide] and ran for 90 min at 90 V submerged in an ice-water bath.

Insertion of the mNeonGreen construct was confirmed using PCR amplification (PrimeSTAR® GXL DNA Polymerase, Catalog R050B) on genomic DNA extracted from human embryonic kidney 293T (HEK293T) cells 72 h after electroporation using primers flanking the target site followed by agarose gel electrophoresis. PCR products were loaded into agarose gels (2% agarose, $1\times$ TAE, containing SYBR Safe) and ran for 90 min at 100 V.

Atomic force microscopy

Freeze 'N Squeeze purified DNA nanostructure samples were imaged with a Bruker BioScope Resolve using the ScanAsyst in Air mode. Samples were prepared by applying 6 μl of sample to freshly cleaved mica (Plano GmbH) and 3 min of incubation before the mica was carefully rinsed with ddH_2O and dried with a gentle flow of air. Imaging was performed with ScanAsyst-Air probes at a typical scan rate of around 1 Hz.

oxDNA simulations

Simulations of four distinct versions of 18-helix DNA nanostructured HDR templates were performed using the coarse-grained model oxDNA (25), including 50% Staples, Only Top, Open and Complex. First, the original caDNAno (26) scaffold and staple strand routings of each nanostructure version were converted to the oxDNA model utilizing the tacoxDNA source code (http://tacoxdna.sissa.it/). Then, a multistep relaxation (Supplementary Table S2) was done to obtain an initial geometry for molecular dynamics (MD) simulations. The relaxation steps are required to correct for overstretched bonds that result from the caDNAno to oxDNA conversion and to resemble a more realistic geometry. Once the structures were relaxed, the MD simulations were performed: consisting of 1×10^7 steps for the structures without homology arms and $1.1–2.5 \times 10^8$ steps for the ssDNA, and in structures containing homology arms with a time step of 0.005, which translates to 0.1–2.5 μs in real-time units. All simulations were performed without applying any external forces and implementing the oxDNA2 package and the NVE John thermostat at a temperature of 303 K and a salt concentration equivalent to 0.5 M NaCl. To run the simulations more efficiently, GPU acceleration was implemented using the OSC (Ohio Supercomputer Center) resources. Analysis of the structural properties was performed using the software MagicDNA (27) and Python-based analysis tool package (https://github.com/sulcgroup/oxdna_analysis_tools) (Supplementary Table S3; Supplementary Figures S2, S3, S6, S7, S10, S11, S14, S15, S18, S19, S22, S23, S26, S27 and S29–S34; Supplementary Movies S1–S4). Lastly, UCSF Chimera software was used for image and video rendering (Figure 1C; Supplementary Figures S1, S5, S9, S13, S17, S21, S25 and S28) (28).

Cell culture

HEK293T and K562 cells were cultured with 10% fetal bovine serum (FBS; VWR) and 1% penicillin/streptomycin (Gibco) at 37°C in a 5% CO_2 air incubator. HEK293T cells were cultured in DMEM (Corning), and K562 cells were cultured in RPMI-1640 (Gibco) media. Routine checks for mycoplasma contamination were performed using the MycoAlert mycoplasma detection kit (Lonza).

Transfections

Transfection was performed using Lipofectamine 3000 (Thermo Fisher Scientific) according to the manufacturer's instructions. Fifty thousand cells per well were seeded in 24-well plates 24 h prior to lipofection. Cells were transfected with 500 ng Cas9 expression plasmid, 150 ng single-guide RNA (sgRNA) expression plasmid, and 0.5 pmol of unstructured ssDNA, looped or 18-helix nanostructures per well.

The Cas9 expression plasmid was constructed by amplifying Cas9 from pMJ920 (Addgene plasmid #42234), and In-Fusion Cloning (Takara Bio) was used to clone Cas9 into the pCAGGS expression vector. Oligos encoding sgRNA spacers (IDT) were phosphorylated, annealed and ligated into digested U6-sgRNA expression vectors.

RNP electroporation

Cas9 RNPs were formulated as previously described (29). In brief, immediately prior to electroporation sgRNA (IDT) was resuspended in IDT duplex buffer to 80 μM and combined with polyglutamic acid sodium salt (Alamanda Polymers, CAS #26247-79-0) dissolved in ddH_2O to 125 mg/ml at a ratio of 1:0.8 sgRNA to PGA. sgRNA/PGA mix and Cas9-NLS (UC Berkeley QB3 MacroLab, stock at 40 μM) were then mixed at a 2:1 molar ratio and incubated at 37°C for 15 min to form Cas9 RNPs at a final concentration of 13.3 μM. Four microliters of complexed RNPs were then incubated with different amounts of HDR templates for 5 min prior to electroporation. Electroporation was performed using a 96-well format 4D nucleofector (Lonza) with 200 000 cells per well. HEK293T cells were electroporated with the SF buffer and the CM-130 pulse code, K562 cells with SF buffer and the FF-120 pulse code, and T cells with the P3 buffer and the EH-115 pulse code. Cells were immediately resuspended in pre-warmed media, incubated for 20 min and transferred to culture plates.

Flow cytometry

Primary human T cells were collected 5 days after electroporations, resuspended in FACS buffer, and stained with Ghost Dye Red 780 (Tonbo), anti-human CD4-PerCP (Tonbo, Cat #67-0047-T500) and anti-human CD25-BV421 (Biolegend, Cat #302630). All primary human T-cell gating strategies included singlet gating, live–dead differentiation, and CD4 and CD8 T-cell differentiation and excluded subcellular debris. All quantified data for experiments using primary human T cells were collected from gated CD4+ T cells only.
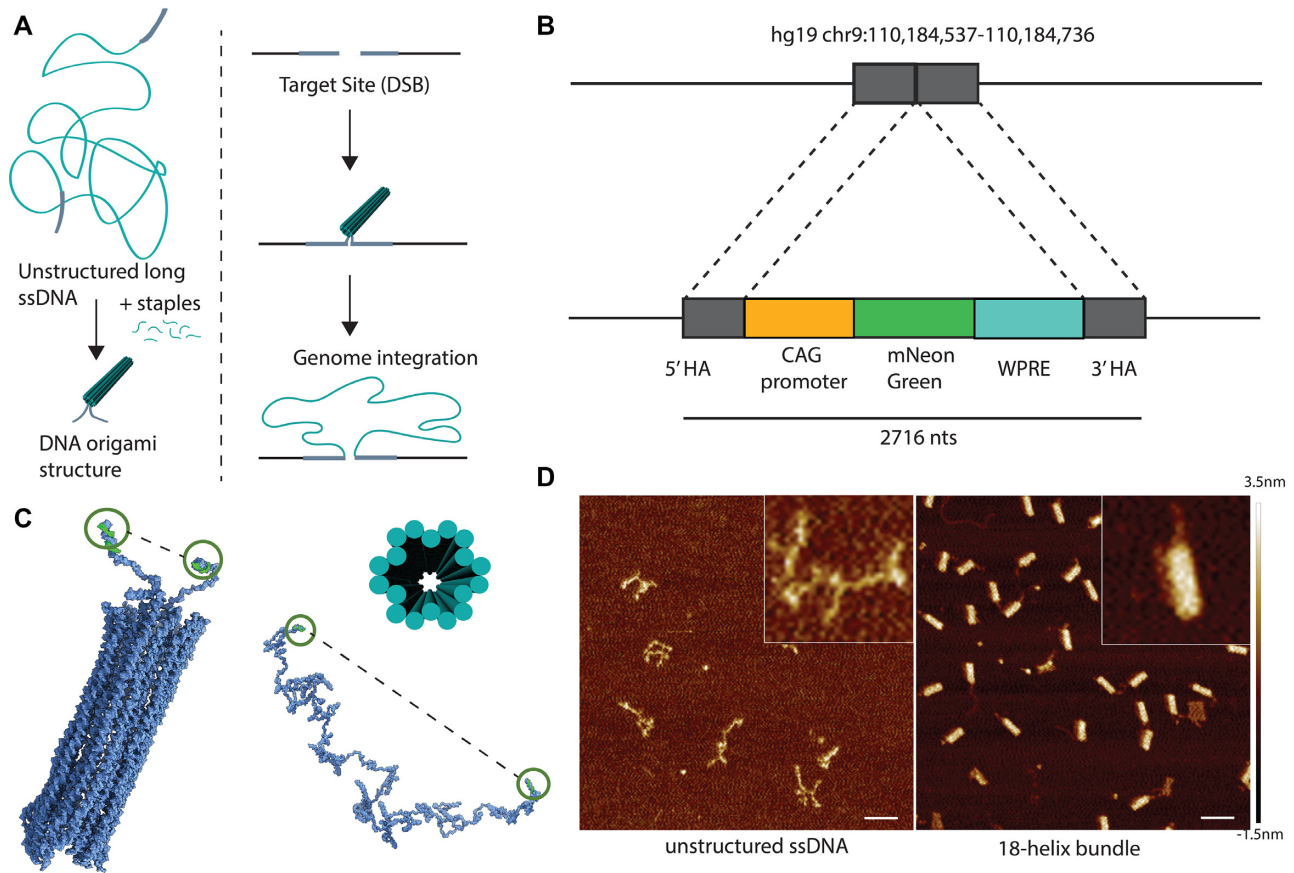
Figure 1. DNA nanostructure encoding mNeonGreen for human genome integration. (**A**) Graphical strategy depiction showing folding of a long unstructured ssDNA into a DNA nanostructure for integration into the genome via CRISPR–Cas9-mediated HDR. (**B**) Schematic of a 2716-base long template encoding mNeonGreen along with regulatory elements and two 100-base homology arms for genome targeting at an intergenic site on human chromosome 9. (**C**) Cylindrical model and oxDNA simulations of an 18-helix bundle DNA nanostructure show a decrease in end-to-end distance from 108.98 ± 11.22 nm (ssDNA) to 29.33 ± 9.9 nm (18-helix). (**D**) AFM characterization of the unstructured ssDNA and the 18-helix DNA nanostructure. Scale bar: 100 nm.

Cells were resuspended in FACS buffer (1% bovine serum albumin in phosphate-buffered saline) and analyzed by flow cytometry for mNeonGreen+ cells 7 days post-transfection. Flow cytometry was performed on an Attune NxT flow cytometer with a 96-well autosampler (Thermo Fisher Scientific), and data analysis was performed using the FlowJo v10 software.

Illumina deep sequencing analysis

DNA was extracted 3 days post-transfection using Quick-Extract DNA Extraction Solution (Lucigen) and heated at 65°C for 20 min followed by 95°C for 20 min. DNA samples were then amplified with PrimeSTAR GXL DNA Polymerase (Takara Bio) with PCR forward/reverse primers containing Illumina adapter sequences for 30 cycles (98°C for 10 s, 55°C for 15 s and 68°C for 1 min).

The resulting amplicons were purified by adding 25 μl of amplicon to 45 μl of SPRI beads (UC Berkeley Sequencing Core). The samples were washed twice with 200 μl of 70% ethanol and eluted in 40 μl of Tris–EDTA buffer (Corning).

The purified samples were sequenced on an Illumina iSeq by QB3 Genomics at UC Berkeley. NGS sequencing reads were analyzed for HDR-mediated genomic integration using CRISPResso2 (https://crispresso.pinellolab.partners.org) in batch mode using default parameters.

Truncated Cas9 target sequences (shuttles)

Truncated Cas9 target sequences (shuttles) were designed based on published guidelines (29,36). In brief, shuttles include a protospacer adjacent motif (PAM) followed by a 20-base sequence designed to have complementarity to the target sequence with the 4 most PAM distal bases switched to other bases; this allows Cas9 RNPs to bind but not cut (29,36). Two different shuttles were used in this study; both were added during DNA nanostructure formation and treated as an additional staple strand. For mNeonGreen constructs, the shuttles were created as hairpins that bind to the ends of the template with the following sequences:

mNeonGreen_Shuttle_1: GCTTACTTGCAGCAGA
AATACCGTCACGTGCTCAGTCTGAATTGCAGA
ATTCAGACTGAGCACGTGACGG

mNeonGreen_Shuttle_2: CCGTCACGTGCTCAGTCT
GAATTGCAGAATTCAGACTGAGCACGTGACGG
AGTATCCCGGTGCAGGAGCT

For the experiments at the CD25 locus in human primary T cells, the shuttle sequence was cloned to the ends of the template as described in previous reports (29,36). During DNA nanostructure folding, a complementary oligo was added to make the shuttles dsDNA and allow Cas9 RNPs to bind.

23–23: 5′RC_CD25-GFP (shuttle 1): GCACTCTCTTCT CTCATCTCCCGGCTGATGTGGGGACTGGAGT

23–26: 3′RC_CD25-GFP (shuttle 2): ACTCCAGTCC CCACATCAGCCGGtgagaaacctgctcatcggg

Primary human T-cell culture

Leukapheresis products from anonymous healthy human donors were purchased from STEMCELL Technologies, Inc. and isolated using an EasySep human T-cell isolation kit (Cat #17951). Isolated CD3$^+$ T cells were activated at 1×10^6 cells/ml in a 1:1 ratio with CD3/CD28 magnetic dynabeads (CTS, Thermo Fisher Scientific), 100 U/ml IL-7 and 10 U/ml IL-15 (R&D Systems) for 48 h in complete XVivo15 medium (Lonza) (5% FBS, 50 μM 2-mercaptoethanol, 10 mM *N*-acetyl L-cysteine). Following the 48-h activation period, CD3$^+$ T cells were debeaded with an EasySep magnet (STEMCELL Technologies, Inc.) prior to resuspension and electroporation at $0.5–1 \times 10^6$ cells/ml in P3 buffer (Lonza). Following electroporations with RNPs and HDR templates, fresh medium and cytokines were added every 2–3 days.

Cas9-VLPs

Cas9-VLPs were harvested from transfected Lenti-X cells. Cultured cells were transfected with 1 μg VSV-G, 3.3 μg psPax2, 6.7 μg Gag-Cas9 and 10 μg U6-ELS77 plasmids using polyethylenimine (Polyscience Inc.). Transfected cells were switched into Optimem (Gibco) 12 h post-transfection and supernatants were harvested 48 h after media change. Supernatants were pooled and filtered through a 0.45-μm aPES filter bottle (Thermo Fisher Scientific). Filtered samples were then concentrated via ultracentrifugation for 2 h at 25 000 rpm on a 30% sucrose cushion. Concentrated VLPs were resuspended in 20 μl SE buffer (Lonza) and electroporated with 4–8 μl of 0.5 pmol/μl HDR template using a 4D Nucleofector with pulse code CM-150 (Lonza). Electroporation of VLPs with HDR templates previously showed improved knock-in efficiencies (30). VLP/template mix was added to 15 000 cells in 50 μl DMEM + 10% FBS and 1× penicillin/streptomycin. Following a 30-min incubation at 37°C, 75 μl Optimem was added to bring the final well volume to ∼150 μl. Cells were passaged on day 3 to maintain subconfluent culture conditions and analyzed by flow cytometry on day 7 using an Attune NxT (Thermo Fisher Scientific).

RESULTS

Design of a DNA nanostructure encoding mNeonGreen for human genome integration

To test whether DNA nanostructures can enter the nucleus, and whether folding into a compact DNA architecture affects template utility for integration into the human genome, we designed a 2716-nucleotide ssDNA scaffold encoding mNeonGreen (31) (Figure 1A and B; Supplementary Figures S17 and S28). At each end, 100-nucleotide homology arms matched the sequences flanking the intended CRISPR–Cas9 cleavage site, such that the final integrated new sequence would be 2516 bp following successful HDR. In addition to mNeonGreen, the insertion segment includes a transcriptional promoter, a polyadenylation signal and a woodchuck hepatitis virus post-transcriptional regulatory element. Successful integration of the template yields green fluorescent cells (mNeonGreen+), enabling detection of genome integration events.

Following established DNA nanostructure design rules, we created the mNeonGreen integration template as a hollow 18-helix bundle (herein called '18-helix nanostructure') (3,32,33) (Figure 1C). Important design criteria included creating scaffolded DNA origami that are structured during the delivery process but are not too rigid and do not have a larger cross section than the diameter of proteins known to cross the nuclear pore. It was important to us to bring homology arms closer together to test whether this could increase genome integration of large DNA templates. We hypothesized that a structured but less compact design with a hollow center would allow structures to cross into the nucleus more readily and also open up and become integrated into the genome during HDR. Specifically, monolayer DNA origami nanostructures exhibit higher local deformability than rigid, multilayer DNA origamis (34). Furthermore, we designed the 18-helix nanostructure without a seam in the scaffold routing, which allows for a more uniform staple strand routing in terms of staple strand length, continuous duplex regions and crossover density. We performed MD simulations (Supplementary Movies S5–S8) implementing the coarse-grained model oxDNA (25,35) to guide the design process, assessing folded-structure energetics and comparing distances between DNA template termini. Consistent with expectations, the oxDNA simulations predicted that terminal homology sites are farther apart in the unstructured template (109 ± 11 nm) compared to the folded nanostructure (29 ± 10 nm) (Supplementary Figures S31–34; Supplementary Table S3). Analysis by native gel electrophoresis showed that the 18-helix nanostructures migrated as a single species in each case, indicating correct structural formation (Supplementary Figure S35). AFM revealed compacted, uniform DNA structures consistent with the designed properties of the 18-helix nanostructures (Figure 1C and D). Conformations observed in AFM were consistent with simulations for both the unstructured template and folded nanostructures (Supplementary Figures S17–S20 and S28–S30).

Nuclear localization and genome integration of nanostructured DNA

After confirming the 18-helix nanostructures were folded, we next tested whether they can enter the nucleus and integrate into the human genome following genome cleavage by CRISPR–Cas9. Two different DNA delivery strategies were employed using HEK293T cells. First, we transfected 0.5 pmol of 18-helix nanostructures together with plasmids encoding CRISPR–Cas9 and an sgRNA targeting

the aforementioned site on chromosome 9 using Lipofectamine (Figures 1B and 2A). In parallel, we electroporated HEK293T cells with CRISPR–Cas9 RNPs together with 0.5 pmol of 18-helix nanostructures. Both experiments included controls in which either 0.5 pmol of unstructured ssDNA (herein called 'unstructured') or 0.5 pmol of a simple DNA nanostructure where the ends of the ssDNA are connected together through base pairing of several strands to fold the template into a closed loop (herein called 'looped') was used in place of 18-helix nanostructures to provide the HDR template during genome editing (Figure 2A). After 7 days, cells were harvested and analyzed by flow cytometry to assess the percentage of mNeonGreen+ cells. We selected this time point to avoid false positives that could arise from transient expression from the DNA donor template. Results showed that using both modes of delivery, DNA nanostructures can enter the nucleus and become integrated in the genome. However, 18-helix nanostructures delivered by transfection resulted in decreased HDR efficiency relative to unstructured DNA ($1.5 \pm 0.8\%$ versus $4.4 \pm 0.1\%$, $P < 0.01$, respectively) (Figure 2B and C). When using electroporation, HDR levels were more similar for both 18-helix nanostructure templates and unstructured templates ($4.0 \pm 0.0\%$ versus $5.5 \pm 0.3\%$, $P < 0.01$, respectively) (Figure 2B and C). Interestingly, the closed looped nanostructure, in which homology arms are proximal but the template itself is unstructured, resulted in a statistically significant increase in HDR efficiency in electroporated samples compared to unstructured DNA ($7.0 \pm 0.4\%$ versus $5.5 \pm 0.3\%$, $P < 0.01$, respectively) (Figure 2B and C). We used primers flanking the Cas9 cleavage site to confirm insertion of the mNeonGreen construct at the expected position (Figure 2D). Additionally, we performed high-throughput sequencing at the junctions between the template and the insertion locus. Sequencing revealed similar insertion and deletion patterns and percentages between unstructured, looped and 18-helix nanostructures at all junctions. Importantly, insertion of staple strand sequences was not observed at these sites (Supplementary Figure S41). To determine whether electroporation affects DNA nanostructural integrity, we diluted 18-helix nanostructures in electroporation media and electroporated half of the sample. AFM revealed that DNA nanostructures maintained integrity after electroporation (Figure 2E; Supplementary Figures S39 and S40). These results suggest that DNA nanostructures can be delivered into the nucleus through electroporation and serve as templates for CRISPR–Cas9-mediated HDR.

Increased HDR efficiency upon CRISPR–Cas9 RNP localization at template DNA ends

These results demonstrate that electroporation is effective at delivering nanostructured DNA to the nucleus. We next investigated whether adding truncated Cas9 target sequences (shuttles) to DNA nanostructures could enhance the rate of nuclear localization and subsequent genome integration (29,36) (Figure 3A). Our results showed that sequence shuttles increase HDR efficiencies for all types of templates tested. We observed $11 \pm 0.4\%$, $12 \pm 0.3\%$ and $10 \pm 0.6\%$ HDR efficiencies using 1 pmol of unstructured, looped or

18-helix nanostructures, respectively (Figure 3B). To determine whether Cas9 RNPs bind directly to the DNA nanostructures as intended (37–39), we incubated the DNA with RNPs and used AFM to analyze the resulting samples. The images reveal Cas9 RNPs bound to the side of the 18-helix nanostructure, where the homology arms and the shuttle sequences are visibly located (Figure 3C; Supplementary Figures S37 and S38). We also investigated whether this strategy could be used to deliver nanostructured DNA into a different cell type. We electroporated synchronized human immortalized myelogenous leukemia K562 cells with Cas9 RNPs alongside unstructured, looped or 18-helix nanostructures including shuttle sequences. We observed similar HDR efficiencies with all templates at a concentration of 1 pmol: $5 \pm 0.8\%$, $5 \pm 0.5\%$ and $4 \pm 0.7\%$ for the unstructured, looped or 18-helix nanostructures, respectively (Figure 3D). Overall, these results demonstrated that shuttle sequences can increase the rate of nanostructured DNA incorporation into the genome in different cell lines and at similar levels relative to unstructured ssDNA templates.

Nanostructured DNA comprising a human gene enhances human primary cell HDR compared to unstructured dsDNA

We next investigated nanostructured DNA delivery into primary human T cells using an ∼3.5-kb multigene cassette targeting *IL2RA*, a gene mutated in some families with a monogenic immune disorder that is potentially amenable to gene replacement strategies (OMIM 606367) (40–42). An ssDNA scaffold composed of two ∼300-bp homology arms flanking the entire *IL2RA* open reading frame, fused to a GFP-encoding sequence and a separate mCherry-encoding sequence, was tested as an HDR template (Figure 4A). Insertion of this HDR template into the genome results in co-expression of a detectable IL2RA–GFP fusion protein driven by the endogenous IL2RA promoter and a separate mCherry protein driven by the EF1a promoter. GFP expression alone would indicate truncated insertion, and expression of mCherry alone could indicate either truncation or insertion into an off-target genomic locus. Because DNA origami structure designs are sequence agnostic, we were able to use a similar 18-helix nanostructure that maintains the same overall geometry and underlying scaffold and staple strand routing as above, which means the crossover density and staple strand lengths are the same. We thus expect the stability and resistance to electroporation for these structures to remain the same. Four different versions of these DNA nanostructures were created with an alternating pattern of base pairing (50% Staples), 18-helix nanostructure restricted to the top half where the homology arms are located (Only Top), an open sheet-like structure (Open) and the full 18-helix nanostructure (Complex) (Figure 4B) (Supplementary Figures S1–S16). We also tested a looped structure comprising only five short oligonucleotide-directed helices, an unstructured ssDNA (Supplementary Figure S24) and an unstructured dsDNA for comparison. All HDR templates included shuttle sequences, and we used electroporation along with Cas9 RNPs on primary human T cells from two different human blood donors for this experiment. All DNA nanostructures demonstrated similar DNA in-
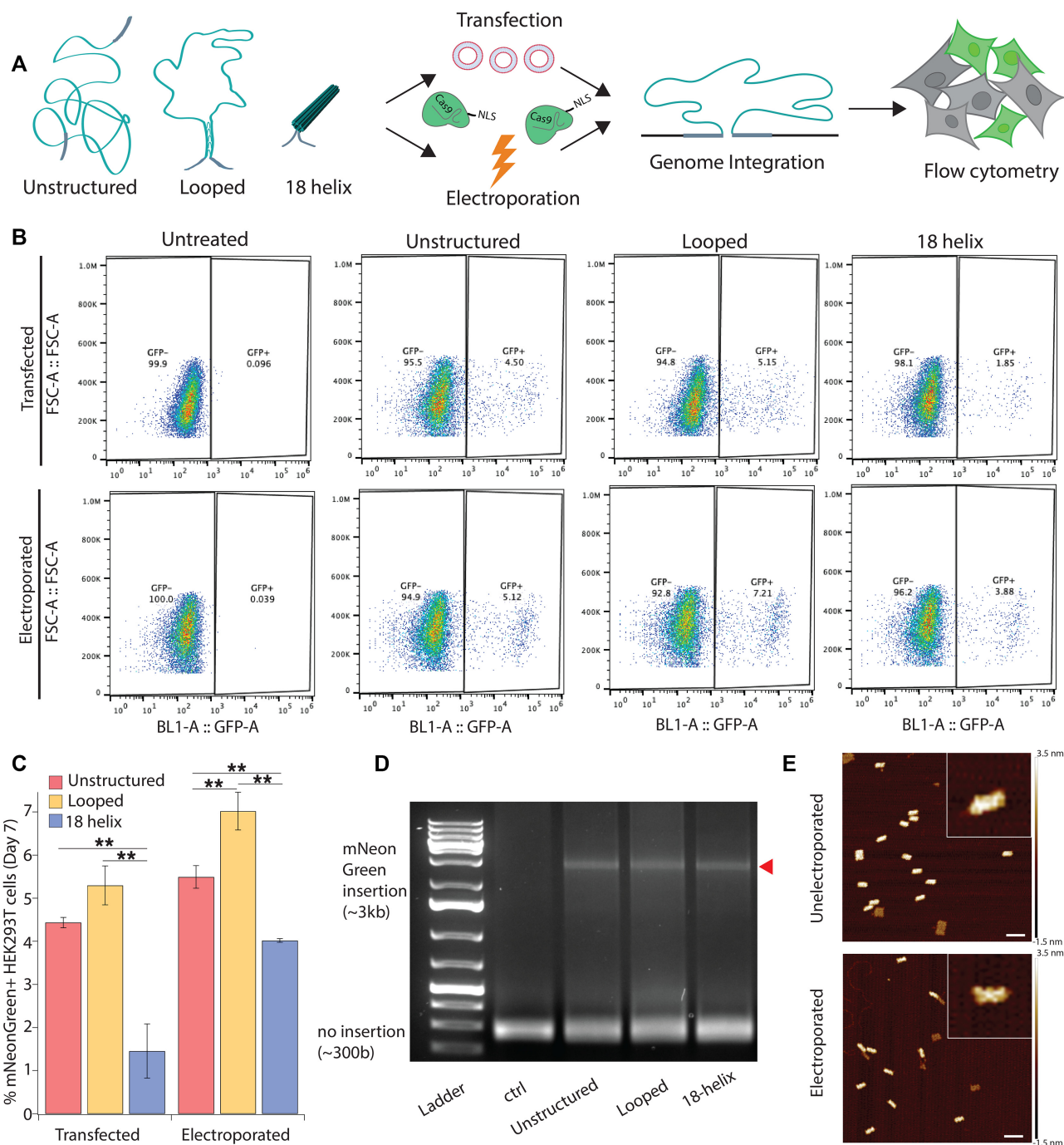
Figure 2. Nuclear localization and genome integration of nanostructured DNA. (**A**) Schematic of experimental approach: 0.5 pmol of each template either was transfected with 500 ng Cas9 nuclease expression plasmid along with 150 ng of sgRNA expressing plasmid or electroporated with 57.2 nmol of Cas9 RNPs. Genomic integration was assessed via flow cytometry after 7 days. (**B**) (i) Flow cytometry data measuring mNeonGreen+ cells (GFP+) show that looped templates are more efficiently incorporated into the genome compared to unstructured and 18-helix nanostructures. (ii) Flow cytometry of electroporated cells shows similar values across unstructured, looped and 18-helix nanostructures. (**C**) Aggregated flow cytometry data show that looped templates perform best for both transfection and electroporation. Error bars represent standard deviations (SDs) from three experiments, **$P < 0.01$, one-way ANOVA. (**D**) PCR using primers flanking the insertion site confirms mNeonGreen insertion at the target site (right triangle). (**E**) AFM images of the 18-helix nanostructure before and after electroporation. Scale bar: 100 nm.
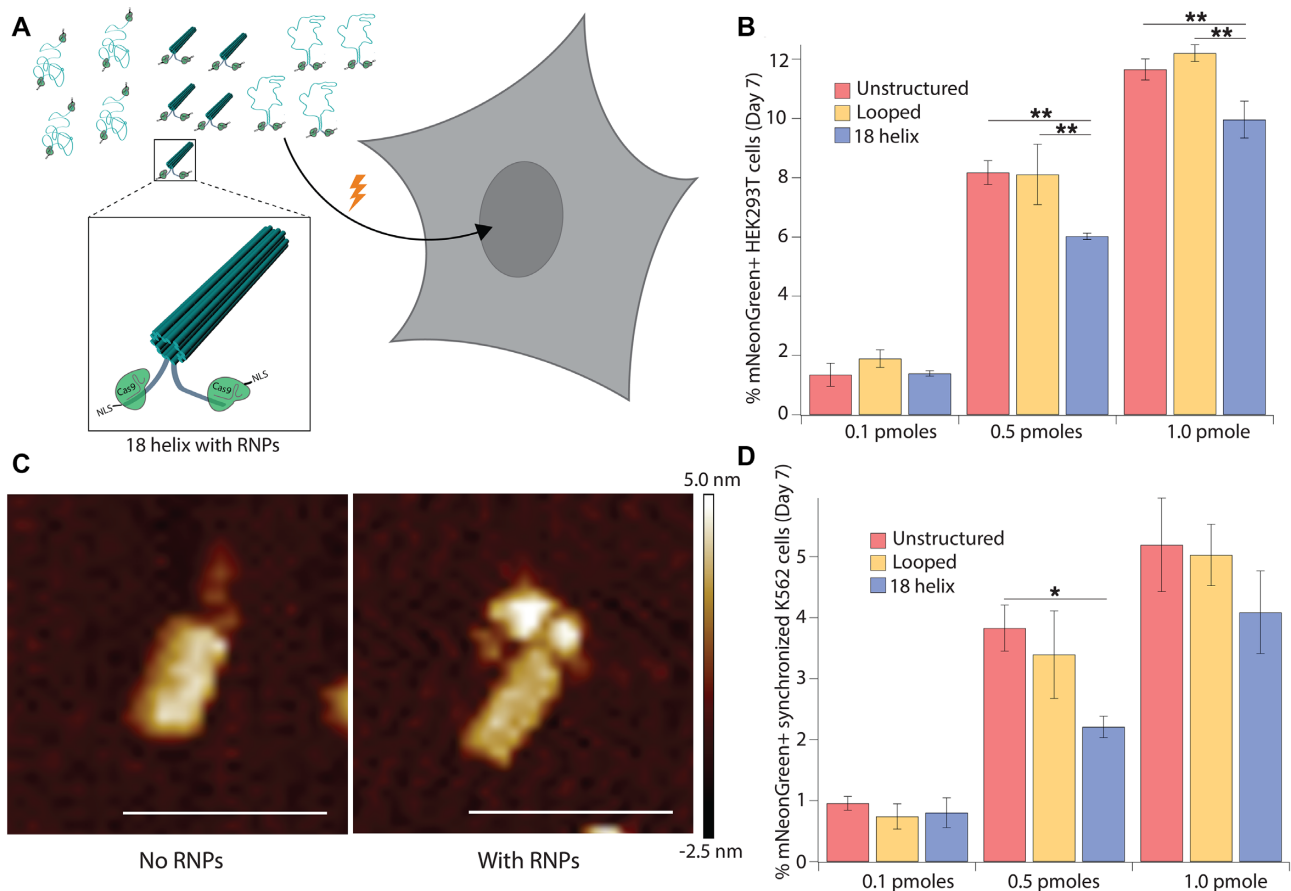
Figure 3. CRISPR–Cas9 RNP localization at template DNA ends increases HDR efficiency. (**A**) Schematic of CRISPR–Cas9 binding to the ends of unstructured, looped and 18-helix nanostructure templates. CRISPR–Cas9 carries nuclear localization signals (NLS) to enter the nucleus upon electroporation. (**B**) Aggregated flow cytometry data show that knock-in efficiencies are similar across unstructured, looped and 18-helix nanostructure templates when electroporating templates bound by CRISPR–Cas9 RNP. Error bars represent SDs from three experiments, **$P < 0.01$, one-way ANOVA. (**C**) AFM image depicting CRISPR–Cas9 RNPs (i) unbound and (ii) bound to 18-helix DNA nanostructures. Scale bar: 100 nm. (**D**) Experiments in synchronized K562 cells show comparable knock-in efficiencies across unstructured, looped and 18-helix nanostructures. Error bars represent SDs from three experiments, *$P < 0.05$, one-way ANOVA.

sertion efficiencies compared to long unstructured ssDNA, consistent with our results in HEK293T and K526 cells (Figures 3 and 4C). In line with previous reports, ssDNA templates demonstrated lower toxicity and higher HDR efficiency relative to dsDNA controls (43,44) (Figure 4C). Importantly, we observed similar numbers across all templates of mCherry+ GFP− and mCherry− GFP+ cells (1–4%), suggesting no differences in off-target integrations, incomplete insertions or imperfect HDR leading to frameshifts or truncations among the different templates (Supplementary Figure S42). Interestingly, although the DNA nanostructures comprised folded dsDNA segments, they caused less toxicity than the unstructured dsDNA templates tested here (Figure 4D). A possible explanation is that the compact nature of the DNA nanostructures, where dsDNA helices are packed closely together and thus are less accessible, may circumvent mechanisms driving the toxicity of free dsDNA. Overall, these results demonstrated that complex DNA nanostructures can be used to compress large ssDNA HDR templates and can mediate efficient insertion in primary human T cells at endogenous target loci.

VLPs enable intracellular delivery of nanostructured DNA

We investigated whether compaction of ssDNA HDR templates in the form of DNA nanostructures can improve their delivery into HEK293T cells using Cas9-VLPs (30). To this end, we delivered shuttled unstructured, looped and 18-helix nanostructure mNeonGreen HDR templates (Figure 1B) into HEK293T cells either by electroporation or by using Cas9-VLPs (Figure 5A). On day 7 after delivery, we collected and analyzed the cells using flow cytometry to track mNeonGreen+ cells. Consistent with previous results, the unstructured and structured DNAs introduced by electroporation yielded similar HDR efficiencies of ∼15% in each case. Although VLP delivery reduced overall HDR levels, we observed a 2.5-fold increase in HDR efficiency for the 18-helix nanostructure templates (from < 2% to > 5%) compared to unstructured and looped templates. These results show that nanostructured DNA can be delivered using VLPs, providing the possibility of *in vivo* delivery for therapeutic or bioimaging purposes into specific tissues. Furthermore, these data demonstrated higher HDR efficiencies when combining Cas9-VLPs and nanostructured HDR
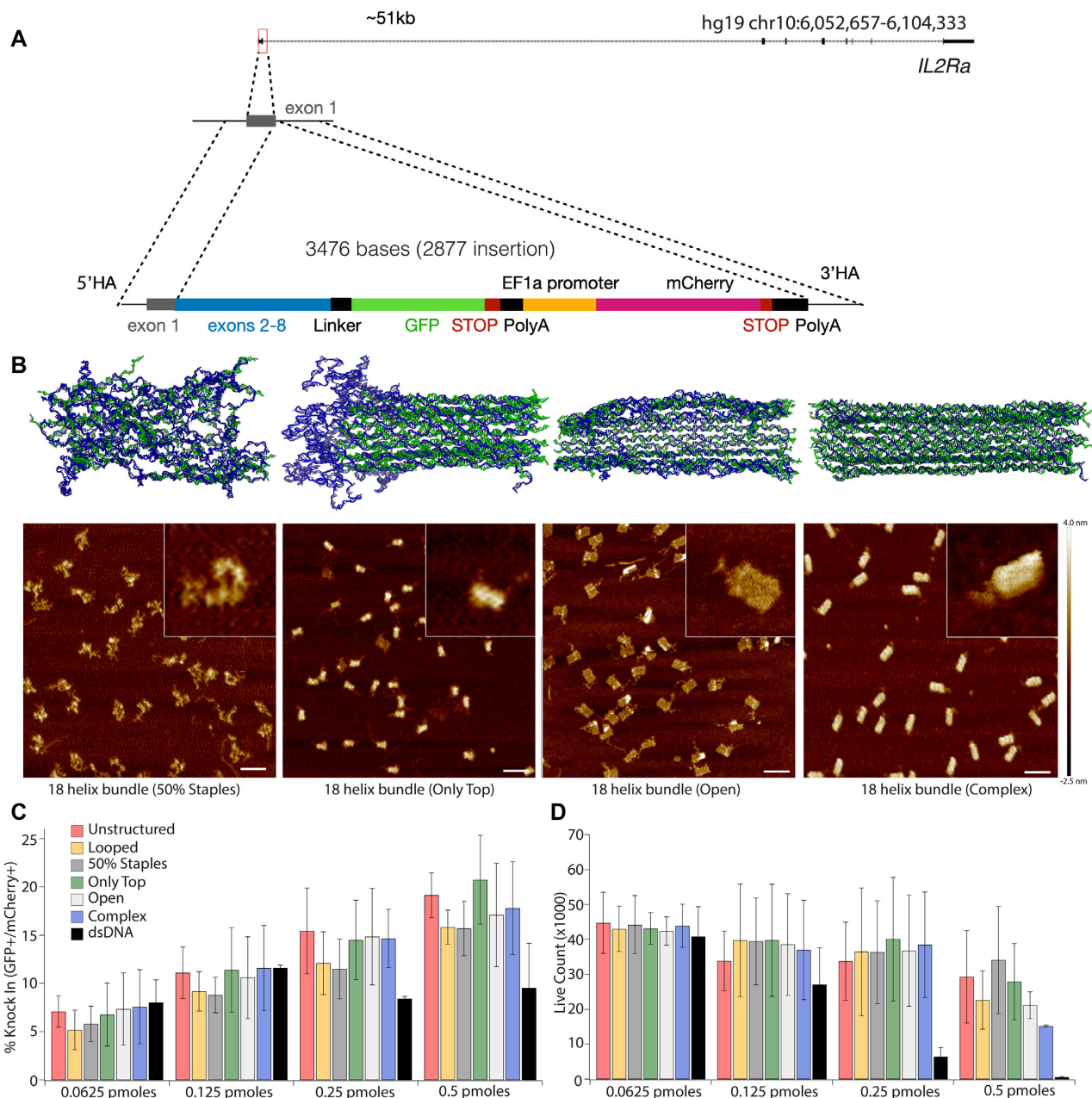
Figure 4. Nanostructured DNA comprising a human gene enhances human primary cell HDR compared to unstructured dsDNA. (**A**) Schematic of knock-in strategy of a 3.5-kb HDR template encoding *IL2RA*–GFP fusion and mCherry driven by an EF1a promoter. (**B**) oxDNA simulations and AFM images of four distinct versions of 18-helix DNA nanostructured HDR templates, including 50% Staples, Only Top, Open and Complex. Scale bar: 100 nm. (**C**) Unstructured ssDNA and 18-helix nanostructure templates show increased knock-in efficiency compared to dsDNA. Error bars represent SDs from duplicate experiments. (**D**) Live cell count shows that unstructured ssDNA and 18-helix nanostructured templates display lower toxicity compared to dsDNA. Error bars represent SDs from duplicate experiments.

templates, an important step toward creating *in vivo* gene replacement or modification therapies.

DISCUSSION

Programmed self-assembled DNA nanostructures have the ability to carry both engineered design features and genetic information, offering a route to creating novel therapeutic approaches and improving genome engineering methods. To date, versatile DNA nanostructures have been cre-

ated, displaying 3D structure, curvature, reconfiguration, modular design and hierarchical assembly into micrometer arrays (5,27,45). Despite these design advances, their ability to carry genetic information has been largely ignored. Nonetheless, potential in cell applications of DNA nanostructures have been discussed since their inception. In particular, *in vivo* use of DNA nanostructures for drug delivery was one of their first proposed applications (46). However, progress has been hampered by challenges, including cellular uptake and the stability of structures in cells (12). DNA
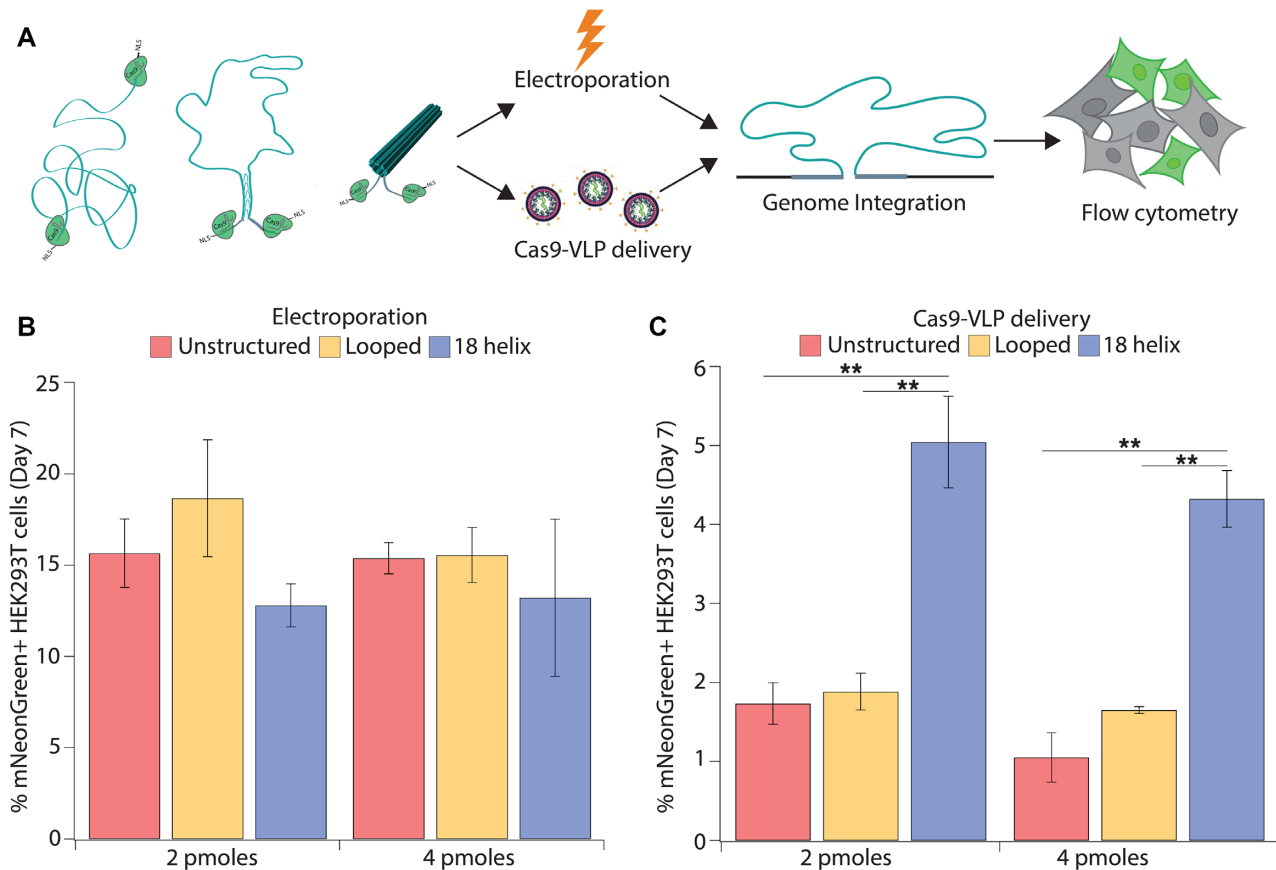
Figure 5. VLPs enable intracellular delivery of nanostructured DNA. (**A**) Schematic of experimental setup where successful incorporation of HDR templates results in mNeonGreen+ cells. (**B**) Knock-in efficiencies of unstructured, looped and 18-helix nanostructures show comparable values for delivery using electroporation. Error bars represent SDs from duplicate experiments. (**C**) Cas9-VLP delivery shows that 18-helix nanostructured templates display a 2.5-fold higher knock-in efficiency compared to unstructured and looped templates. Error bars represent SDs from duplicate experiments, $**P < 0.01$, one-way ANOVA.

nanostructures have demonstrated promise for the delivery of molecular payloads including small molecule drugs, nucleic acids, peptides and proteins *in vitro* (14,20,47–49) and *in vivo* (11,17,50–52). These studies utilize the DNA nanostructure as a carrier, taking advantage of the ability to precisely incorporate these molecules on internal or external surfaces. Here, we leveraged the ability to package a gene-length sequence, making the information encoded in the nanostructure itself the payload. In contrast to prior studies, gene delivery requires entry to cell nuclei, which has not been previously demonstrated. A recent study showed successful electroporation of DNA nanostructures into mammalian cells (13) but only demonstrated delivery into the cytosol.

Here, we describe the use of nanostructured DNAs as templates for HDR-mediated genome editing using CRISPR–Cas9, providing a strategy for DNA compaction and localization that could expand CRISPR applications. This is the first instance of DNA nanostructures generated from scaffolds containing genes that could be delivered into human cells by electroporation or using Cas9-VLPs. The mechanism and timing of DNA nanostructure unpacking and incorporation are important follow-up questions to this work, and understanding how design features affect nuclear

localization and incorporation efficiency could likely guide improved nanostructure designs for delivery and integration of HDR templates. We found that addition of truncated Cas9 target site sequences onto the ends of the nanostructured DNA improves HDR efficiency, presumably due to enhanced template localization to the site of genome repair following Cas9 cleavage (29,36). Furthermore, nanostructured DNA could be delivered into primary human T cells and used as donor templates for gene replacement following Cas9-catalyzed genome cleavage. Finally, we observed higher HDR efficiency for nanostructured versus unstructured DNA templates when delivered by VLPs, opening the possibility of introducing nanostructured DNA templates *in vivo* in a tissue-specific manner for therapeutic applications.

Truncated Cas9 target sequences can increase template delivery into the nucleus and increase HDR efficiency of DNA templates (29,36). AFM experiments showed that Cas9 associates with these sequences, which may induce enhanced template localization as passengers during nuclear import of Cas9 RNPs. Enhanced Cas9-induced HDR with tag-containing DNA templates was observed in multiple cell types, including HEK293T, K562 and human primary T cells. Notably, although higher HDR levels and lower tox-

icity occurred with nanostructured DNA compared to unstructured dsDNA templates, we did not observe increased HDR efficiency compared to unstructured ssDNA templates. This suggests that HDR efficiency may be further increased by changing design features of the nanostructures, pending insight into the mechanisms underlying nuclear localization and genomic integration of structured DNA.

Nanostructured DNA delivery using Cas9-VLPs has two primary advantages over electroporation: lower toxicity and the potential for tissue-specific and *in vivo* delivery (30). Our data show a higher HDR efficiency when coupling Cas9-VLPs with DNA nanostructured templates, compared to unstructured ssDNA templates presumably due to enhanced template delivery to the nucleus. How compaction of templates into nanostructures improves VLP delivery remains an open question. However, this strategy offers the potential to deliver DNA nanostructures *in vivo* in a tissue-specific manner, which could enhance bioimaging, radiotherapy and cancer treatment applications. It further allows *in vivo* delivery of large HDR DNA templates in diseases in which a gene replacement at the endogenous site could serve as a universal cure for patients suffering from a wide range of different substitution mutations and deletions on the causal genes.

Together, these findings validate three distinct strategies to deliver nanostructured DNA into cell nuclei and demonstrate their utility as templates for HDR-mediated genome editing. By exploiting their design features together with their capacity to carry genetic information, DNA nanostructures provide a new approach to DNA template-based genetic manipulation that could enable tissue-selective delivery and editing using Cas9-VLPs.

DATA AVAILABILITY

The authors confirm that the data supporting the findings of this study are available within the article and the Supplementary Data.

SUPPLEMENTARY DATA

Supplementary Data are available at NAR Online.

REFERENCES

1. Seeman,N.C. (1982) Nucleic acid junctions and lattices. *J. Theor. Biol.*, **99**, 237–247.
2. Chen,J.H. and Seeman,N.C. (1991) Synthesis from DNA of a molecule with the connectivity of a cube. *Nature*, **350**, 631–633.
3. Rothemund,P.W.K. (2006) Folding DNA to create nanoscale shapes and patterns. *Nature*, **440**, 297–302.
4. Castro,C.E., Kilchherr,F., Kim,D.-N., Shiao,E.L., Wauer,T., Wortmann,P., Bathe,M. and Dietz,H. (2011) A primer to scaffolded DNA origami. *Nat. Methods*, **8**, 221–229.
5. Dey,S., Fan,C., Gothelf,K.V., Li,J., Lin,C., Liu,L., Liu,N., Nijenhuis,M.A.D., Saccà,B., Simmel,F.C. *et al.* (2021) DNA origami. *Nat. Rev. Methods Primers*, **1**, 13.
6. Zhao,Y., Dai,X., Wang,F., Zhang,X., Fan,C. and Liu,X. (2019) Nanofabrication based on DNA nanotechnology. *Nano Today*, **26**, 123–148.

7. Daems,D., Pfeifer,W., Rutten,I., Saccà,B., Spasic,D. and Lammertyn,J. (2018) Three-dimensional DNA origami as programmable anchoring points for bioreceptors in fiber optic surface plasmon resonance biosensing. *ACS Appl. Mater. Interfaces*, **10**, 23539–23547.

8. Funke,J.J., Ketterer,P., Lieleg,C., Korber,P. and Dietz,H. (2016) Exploring nucleosome unwrapping using DNA origami. *Nano Lett.*, **16**, 7891–7898.

9. Le,J.V., Luo,Y., Darcy,M.A., Lucas,C.R., Goodwin,M.F., Poirier,M.G. and Castro,C.E. (2016) Probing nucleosome stability with a DNA origami nanocaliper. *ACS Nano*, **10**, 7073–7084.

10. Wang,Y., Le,J.V., Crocker,K., Darcy,M.A., Halley,P.D., Zhao,D., Andrioff,N., Croy,C., Poirier,M.G. and Bundschuh,R. *et al.* (2021) A nanoscale DNA force spectrometer capable of applying tension and compression on biomolecules. *Nucleic Acids Res.*, **49**, 8987–8999.

11. Li,J., Green,A.A., Yan,H. and Fan,C. (2017) Engineering nucleic acid structures for programmable molecular circuitry and intracellular biocomputation. *Nat. Chem.*, **9**, 1056–1067.

12. Ramakrishnan,S., Ijäs,H., Linko,V. and Keller,A. (2018) Structural stability of DNA origami nanostructures under application-specific conditions. *Comput. Struct. Biotechnol. J.*, **16**, 342–349.

13. Chopra,A., Krishnan,S. and Simmel,F.C. (2016) Electrotransfection of polyamine folded DNA origami structures. *Nano Lett.*, **16**, 6683–6690.

14. Li,J., Fan,C., Pei,H., Shi,J. and Huang,Q. (2013) Smart drug delivery nanocarriers with self-assembled DNA nanostructures. *Adv. Mater.*, **25**, 4386–4396.

15. Madhanagopal,B.R., Zhang,S., Demirel,E., Wady,H. and Chandrasekaran,A.R. (2018) DNA nanocarriers: programmed to deliver. *Trends Biochem. Sci*, **43**, 997–1013.

16. Zhao,S., Duan,F., Liu,S., Wu,T., Shang,Y., Tian,R., Liu,J., Wang,Z.-G., Jiang,Q. and Ding,B. (2019) Efficient intracellular delivery of RNase A using DNA origami carriers. *ACS Appl. Mater. Interfaces*, **11**, 11112–11118.

17. Li,S., Jiang,Q., Liu,S., Zhang,Y., Tian,Y., Song,C., Wang,J., Zou,Y., Anderson,G.J., Han,J.-Y. *et al.* (2018) A DNA nanorobot functions as a cancer therapeutic in response to a molecular trigger *in vivo*. *Nat. Biotechnol.*, **36**, 258–264.

18. Wang,Z., Song,L., Liu,Q., Tian,R., Shang,Y., Liu,F., Liu,S., Zhao,S., Han,Z., Sun,J. *et al.* (2021) A tubular DNA nanodevice as a siRNA/chemo-drug co-delivery vehicle for combined cancer therapy. *Angew. Chem. Int. Ed. Engl.*, **60**, 2594–2598.

19. Zhang,H., Demirer,G.S., Zhang,H., Ye,T., Goh,N.S., Aditham,A.J., Cunningham,F.J., Fan,C. and Landry,M.P. (2019) DNA nanostructures coordinate gene silencing in mature plants. *Proc. Natl Acad. Sci. U.S.A.*, **116**, 7543–7548.

20. Jiao,K., Zhu,B., Guo,L., Zhou,H., Wang,F., Zhang,X., Shi,J., Li,Q., Wang,L., Li,J. *et al.* (2020) Programming switchable transcription of topologically constrained DNA. *J. Am. Chem. Soc.*, **142**, 10739–10746.

21. Beltrán,S.M., Slepian,M.J. and Taylor,R.E. (2020) Extending the capabilities of molecular force sensors via DNA nanotechnology. *Crit. Rev. Biomed. Eng.*, **48**, 1–16.

22. Wang,S., Zhou,Z., Ma,N., Yang,S., Li,K., Teng,C., Ke,Y. and Tian,Y. (2020) DNA origami-enabled biosensors. *Sensors*, **20**, 6899.

23. Wamhoff,E.-C., Banal,J.L., Bricker,W.P., Shepherd,T.R., Parsons,M.F., Veneziano,R., Stone,M.B., Jun,H., Wang,X. and Bathe,M. (2019) Programming structured DNA assemblies to probe biophysical processes. *Annu. Rev. Biophys.*, **48**, 395–419.

24. Wagenbauer,K.F., Engelhardt,F.A.S., Stahl,E., Hechtl,V.K., Stömmer,P., Seebacher,F., Meregalli,L., Ketterer,P., Gerling,T. and Dietz,H. (2017) How we make DNA origami. *ChemBioChem*, **18**, 1873–1885.

25. Šulc,P., Romano,F., Ouldridge,T.E., Rovigatti,L., Doye,J.P.K. and Louis,A.A. (2012) Sequence-dependent thermodynamics of a coarse-grained DNA model. *J. Chem. Phys.*, **137**, 135101.

26. Douglas,S.M., Marblestone,A.H., Teerapittayanon,S., Vazquez,A., Church,G.M. and Shih,W.M. (2009) Rapid prototyping of 3D DNA-origami shapes with caDNAno. *Nucleic Acids Res.*, **37**, 5001–5006.

27. Huang,C.-M., Kucinic,A., Johnson,J.A., Su,H.-J. and Castro,C.E. (2021) Integrated computer-aided engineering and design for DNA assemblies. *Nat. Mater.*, **20**, 1264–1271.

28. Pettersen,E.F., Goddard,T.D., Huang,C.C., Couch,G.S., Greenblatt,D.M., Meng,E.C. and Ferrin,T.E. (2004) UCSF Chimera—a visualization system for exploratory research and analysis. *J. Comput. Chem.*, **25**, 1605–1612.

29. Nguyen,D.N., Roth,T.L., Li,P.J., Chen,P.A., Apathy,R., Mamedov,M.R., Vo,L.T., Tobin,V.R., Goodman,D., Shifrut,E. *et al.* (2020) Polymer-stabilized Cas9 nanoparticles and modified repair templates increase genome editing efficiency. *Nat. Biotechnol.*, **38**, 44–49.

30. Hamilton,J.R., Tsuchida,C.A., Nguyen,D.N., Shy,B.R., McGarrigle,E.R., Sandoval Espinoza,C.R., Carr,D., Blaeschke,F., Marson,A. and Doudna,J.A. (2021) Targeted delivery of CRISPR–Cas9 and transgenes enables complex immune cell engineering. *Cell Rep.*, **35**, 109207.

31. Shaner,N.C., Lambert,G.G., Chammas,A., Ni,Y., Cranfill,P.J., Baird,M.A., Sell,B.R., Allen,J.R., Day,R.N., Israelsson,M. *et al.* (2013) A bright monomeric green fluorescent protein derived from *Branchiostoma lanceolatum*. *Nat. Methods*, **10**, 407–409.

32. Ke,Y., Bellot,G., Voigt,N.V., Fradkov,E. and Shih,W.M. (2012) Two design strategies for enhancement of multilayer–DNA-origami folding: underwinding for specific intercalator rescue and staple-break positioning. *Chem. Sci.*, **3**, 2587–2597.

33. Martin,T.G. and Dietz,H. (2012) Magnesium-free self-assembly of multi-layer DNA objects. *Nat. Commun.*, **3**, 1103.

34. Wang,Y., Benson,E., Fördős,F., Lolaico,M., Baars,I., Fang,T., Teixeira,A.I. and Högberg,B. (2021) DNA origami penetration in cell spheroid tissue models is enhanced by wireframe design. *Adv. Mater.*, **33**, 2008457.

35. Lee,J.Y., Lee,J.G., Yun,G., Lee,C., Kim,Y.-J., Kim,K.S., Kim,T.H. and Kim,D.-N. (2021) Rapid computational analysis of DNA origami assemblies at near-atomic resolution. *ACS Nano*, **15**, 1002–1015.

36. Shy,B.R., Vykunta,V., Ha,A., Roth,T.L., Talbot,A., Nguyen,D.N., Chen,Y.Y., Blaeschke,F., Vedova,S., Mamedov,M.R. *et al.* (2021) Hybrid ssDNA repair templates enable high yield genome engineering in primary cells for disease modeling and cell therapy manufacturing. bioRxiv doi: https://doi.org/10.1101/2021.09.02.458799, 04 September 2021, preprint: not peer reviewed.

37. Jinek,M., Chylinski,K., Fonfara,I., Hauer,M., Doudna,J.A. and Charpentier,E. (2012) A programmable dual-RNA-guided DNA endonuclease in adaptive bacterial immunity. *Science*, **337**, 816–821.

38. Pattanayak,V., Lin,S., Guilinger,J.P., Ma,E., Doudna,J.A. and Liu,D.R. (2013) High-throughput profiling of off-target DNA cleavage reveals RNA-programmed Cas9 nuclease specificity. *Nat. Biotechnol.*, **31**, 839–843.

39. Nuñez,J.K., Harrington,L.B. and Doudna,J.A. (2016) Chemical and biophysical modulation of Cas9 for tunable genome engineering. *ACS Chem. Biol.*, **11**, 681–688.

40. Goudy,K., Aydin,D., Barzaghi,F., Gambineri,E., Vignoli,M., Ciullini Mannurita,S., Doglioni,C., Ponzoni,M., Cicalese,M.P., Assanelli,A. *et al.* (2013) Human IL2RA null mutation mediates immunodeficiency with lymphoproliferation and autoimmunity. *Clin. Immunol.*, **146**, 248–261.

41. Bezrodnik,L., Caldirola,M.S., Seminario,A.G., Moreira,I. and Gaillard,M.I. (2014) Follicular bronchiolitis as phenotype associated with CD25 deficiency. *Clin. Exp. Immunol.*, **175**, 227–234.

42. Bousfiha,A., Jeddane,L., Picard,C., Al-Herz,W., Ailal,F., Chatila,T., Cunningham-Rundles,C., Etzioni,A., Franco,J.L., Holland,S.M. *et al.* (2020) Human inborn errors of immunity: 2019 update of the IUIS phenotypical classification. *J. Clin. Immunol.*, **40**, 66–81.

43. Hornung,V. and Latz,E. (2010) Intracellular DNA recognition. *Nat. Rev. Immunol.*, **10**, 123–130.

44. Roth,T.L., Puig-Saus,C., Yu,R., Shifrut,E., Carnevale,J., Li,P.J., Hiatt,J., Saco,J., Krystofinski,P., Li,H. *et al.* (2018) Reprogramming human T cell function and specificity with non-viral genome targeting. *Nature*, **559**, 405–409.

45. DeLuca,M., Shi,Z., Castro,C.E. and Arya,G. (2020) Dynamic DNA nanotechnology: toward functional nanoscale devices. *Nanoscale Horiz.*, **5**, 182–201.

46. Douglas,S.M., Bachelet,I. and Church,G.M. (2012) A logic-gated nanorobot for targeted transport of molecular payloads. *Science*, **335**, 831–834.

47. Jiang,Q., Song,C., Nangreave,J., Liu,X., Lin,L., Qiu,D., Wang,Z.-G., Zou,G., Liang,X., Yan,H. *et al.* (2012) DNA origami as a carrier for

circumvention of drug resistance. *J. Am. Chem. Soc.*, **134**, 13396–13403.

48. Zhao,Y.-X., Shaw,A., Zeng,X., Benson,E., Nyström,A.M. and Högberg,B. (2012) DNA origami delivery system for cancer therapy with tunable release properties. *ACS Nano*, **6**, 8684–8691.

49. Halley,P.D., Lucas,C.R., McWilliams,E.M., Webber,M.J., Patton,R.A., Kural,C., Lucas,D.M., Byrd,J.C. and Castro,C.E. (2016) Daunorubicin-loaded DNA origami nanostructures circumvent drug-resistance mechanisms in a leukemia model. *Small*, **12**, 308–320.

50. Zhao,S., Tian,R., Wu,J., Liu,S., Wang,Y., Wen,M., Shang,Y., Liu,Q., Li,Y., Guo,Y. *et al.* (2021) A DNA origami-based aptamer nanoarray

for potent and reversible anticoagulation in hemodialysis. *Nat. Commun.*, **12**, 358.

51. Palazzolo,S., Hadla,M., Russo Spena,C., Caligiuri,I., Rotondo,R., Adeel,M., Kumar,V., Corona,G., Canzonieri,V., Toffoli,G. *et al.* (2019) An effective multi-stage liposomal DNA origami nanosystem for *in vivo* cancer therapy. *Cancers*, **11**, 1997.

52. Zhang,Q., Jiang,Q., Li,N., Dai,L., Liu,Q., Song,L., Wang,J., Li,Y., Tian,J., Ding,B. *et al.* (2014) DNA origami as an *in vivo* drug delivery vehicle for cancer therapy. *ACS Nano*, **8**, 6633–6643.